Science Advances
AAAS

advances.sciencemag.org/cgi/content/full/6/34/eaaz2743/DC1

Supplementary Materials for

Laser writing of nitrogen-doped silicon carbide for biological modulation

Vishnu Nair, Jaeseok Yi, Dieter Isheim, Menahem Rotenberg, Lingyuan Meng, Fengyuan Shi, Xinqi Chen, Xiang Gao,
Aleksander Prominski, Yuanwen Jiang, Jiping Yue, Charles T. Gallagher, David N. Seidman, Bozhi Tian*

*Corresponding author. Email: btian@uchicago.edu

Published 21 August 2020, *Sci. Adv.* **6**, eaaz2743 (2020)
DOI: 10.1126/sciadv.aaz2743

The PDF file includes:

Figs. S1 to S10
Legends for movies S1 and S2

Other Supplementary Material for this manuscript includes the following:

(available at advances.sciencemag.org/cgi/content/full/6/34/eaaz2743/DC1)

Movies S1 and S2

Supplementary Figures:

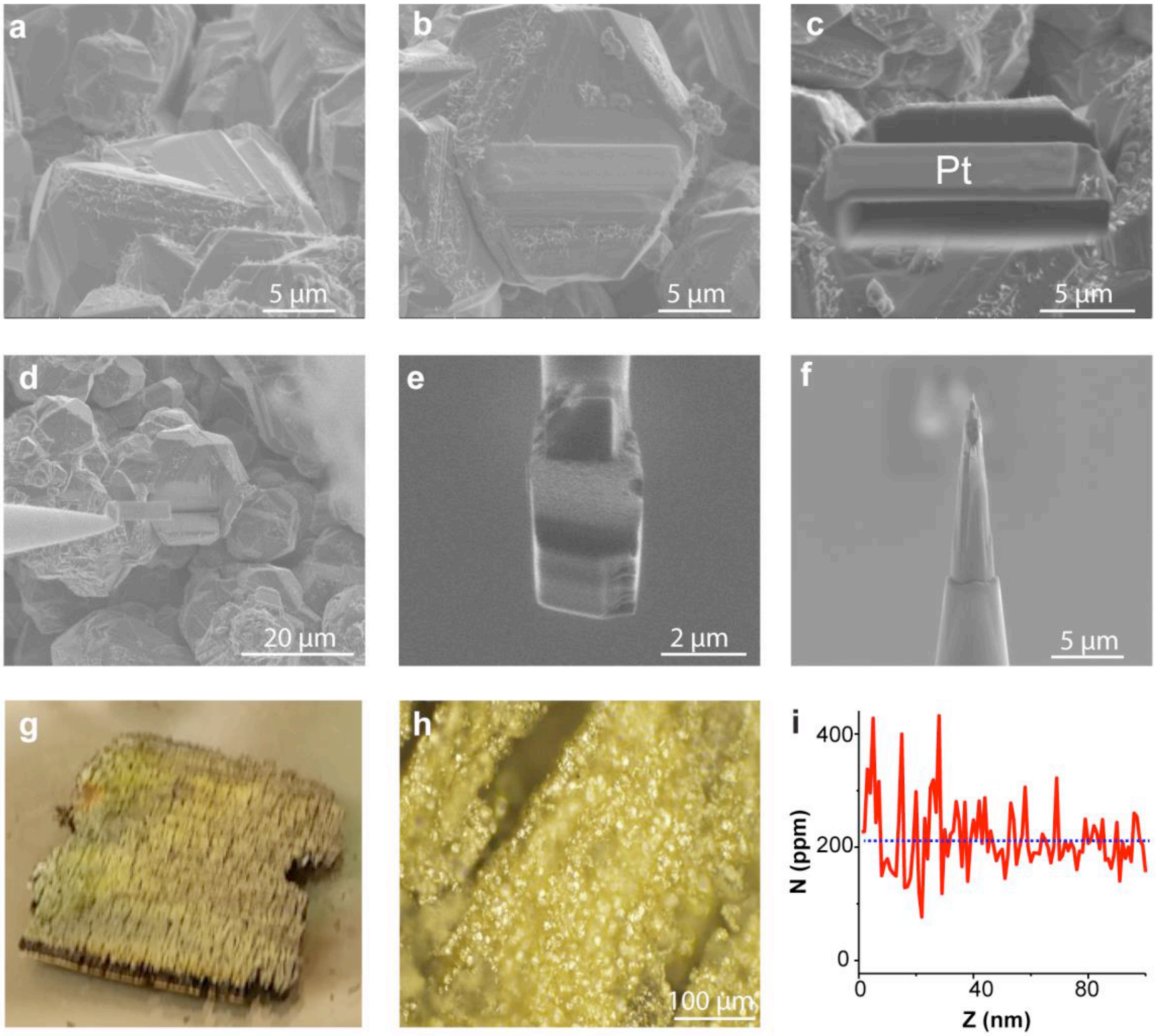

Fig. S1. The composition of the 3C-SiC sample was analyzed by atom probe tomography. a. SEM image of a flat surface identified for FIB preparation of atom probe tomography tips. **b**. Deposition of platinum to protect the sample of interest. **c.** FIB milling of trenches on either side of the sample of interest protected by platinum coating. **d.** Lift out of a lamella using micromanipulator. **e.** FIB image showing a section of lamella, platinum welded on a silicon micropost. **f.** Polished tip for atom probe tomography measurement on a silicon micropost. **g.** Photograph of as synthesized yellow 3C-SiC with graphite layer beneath. Photo credit: Jaeseok Yi, the University of Chicago. **h.** Optical microscopy image of yellow 3C-SiC crystals. Photo credit: Jaeseok Yi, the University of Chicago. **i.** Nitrogen concentration profile along the depth (tip to base) of atom probe tip reconstructed in **Fig. 1F**. The average concentration is indicated at ~ 215 ppm with a dotted blue line**.**

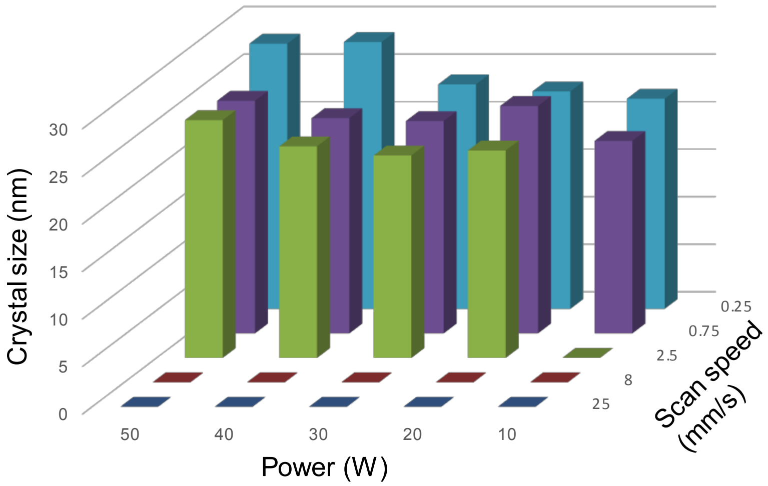

Fig. S2. Crystal size can be controlled by laser power and scan speed. Crystal size as a function of the laser power and scan speed illustrate that the synthesis is all or none and has a cutoff energy density controlled by the synthesis parameters. The crystal sizes were estimated by using Debye-Scherrer equation on the (111) peak of x-ray diffraction.

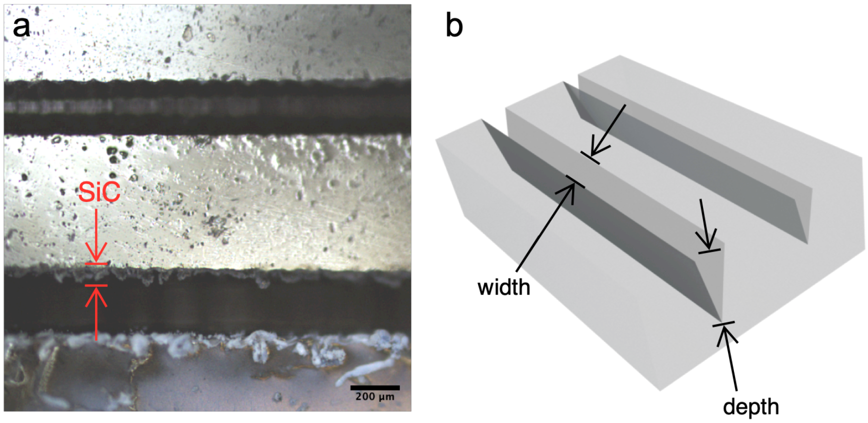

Fig. S3. The printing resolution was estimated by optical microscopy. a. Optical microscopy image from the top of a laser-ablated pattern on PDMS. **b.** Schematic illustration of the 'width' and 'depth' in the laser-produced structure.

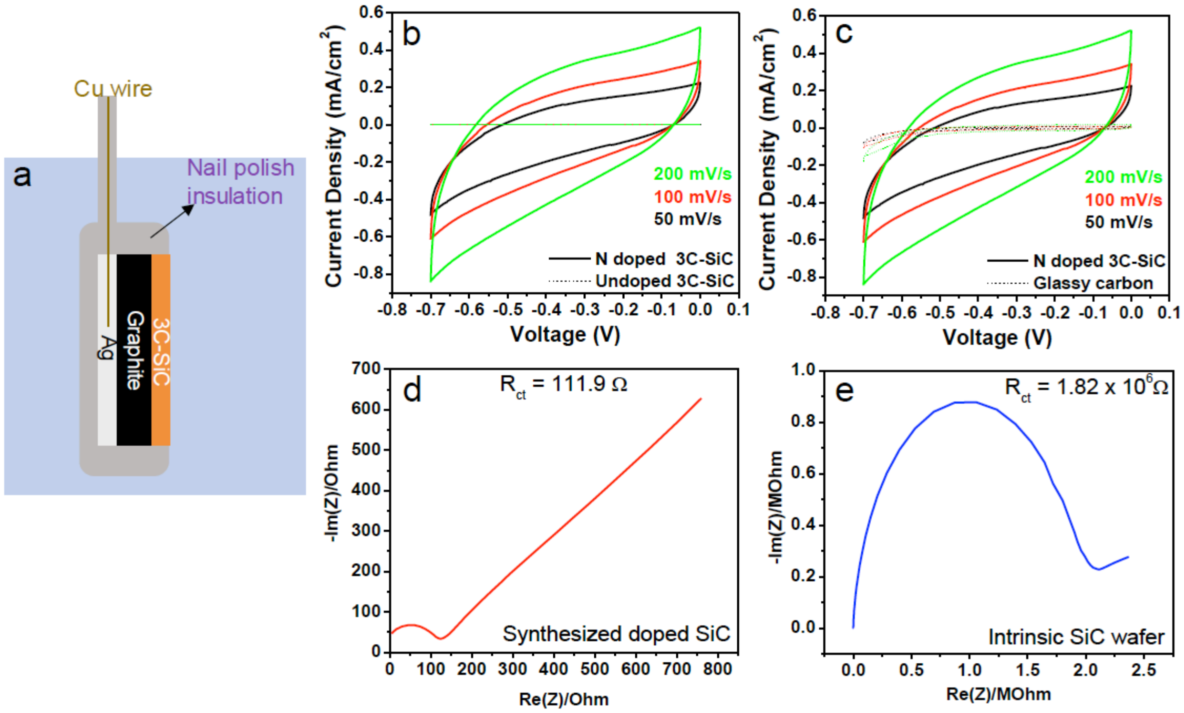

Fig. S4. We characterized the electrochemical properties of the composites with a partially encapsulated device. a. Schematic illustration of the electrode prepared for characterization of its electrochemical properties. The electrode preparation is discussed in detail in the materials and methods section of the manuscript. The utility of 3C-SiC as a pseudocapacitively coupled electrode is demonstrated by the cyclic voltammograms **(b, c)**. A comparison of cyclic voltammograms with undoped 3C-SiC and standard glassy carbon suggest that the faradaic component giving rise to pseudo capacitance arises purely from nitrogen doping of SiC. Furthermore, electrochemical impedance studies suggest that the doped structure **(d)** enables a very low resistance of charge transfer at the electrode-electrolyte interface when compared to intrinsic SiC **(e)**.

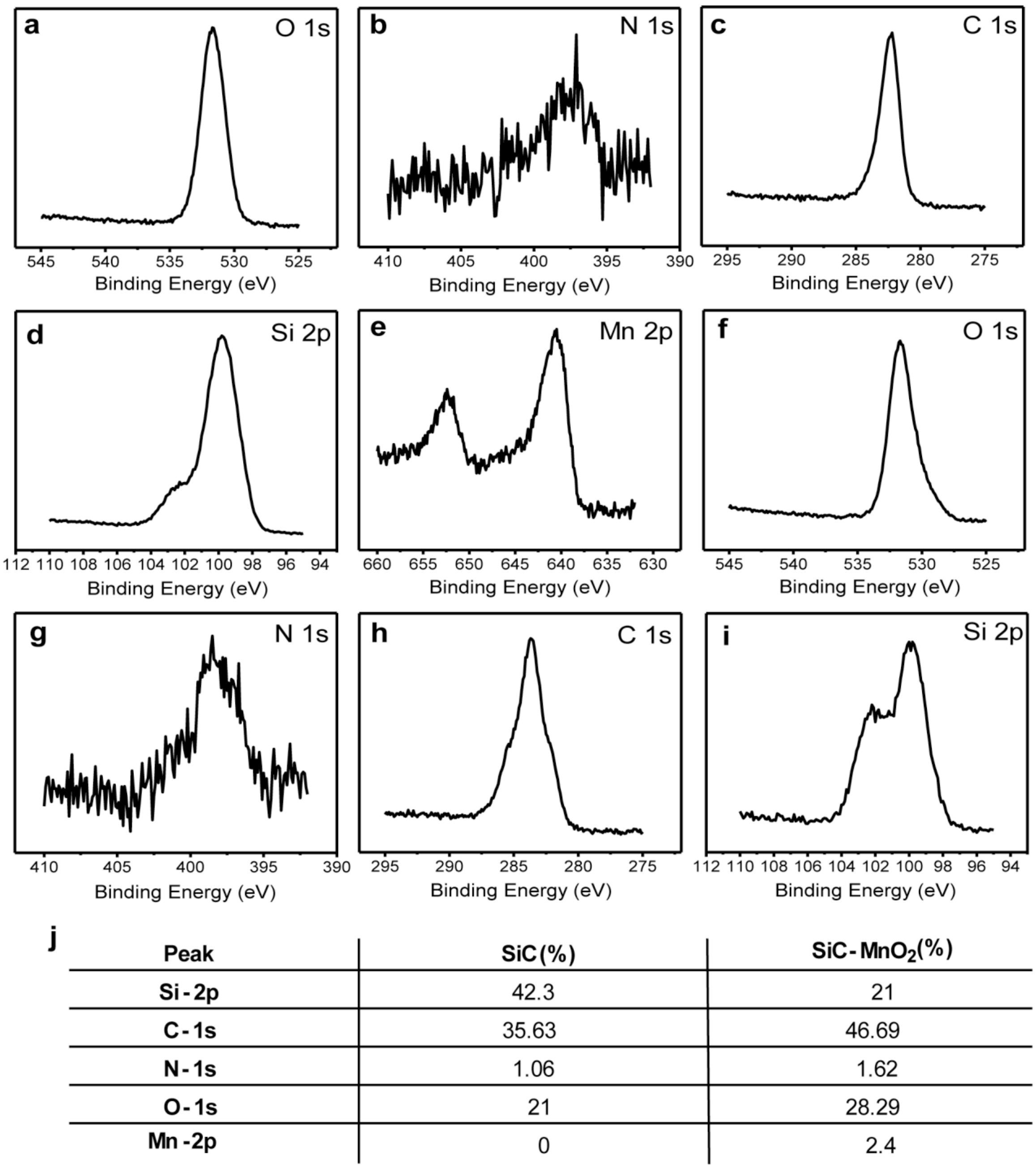

Peak	SiC (%)	SiC-MnO_2(%)
Si-2p	42.3	21
C-1s	35.63	46.69
N-1s	1.06	1.62
O-1s	21	28.29
Mn-2p	0	2.4

Fig. S5. We characterized the surfaces of 3C-SiC and 3C-SiC-MnO2 samples with X-ray photoelectron spectroscopy. Elemental XPS spectrum collected on 3C-SiC samples for **(a)** oxygen 1s**, (b)** nitrogen 1s, **(c)** carbon 1s, **(d)** silicon 2p. and 3C-SiC-MnO_2 samples for **(e)** manganese 2p, **(f)** oxygen 1s, **(g)** nitrogen 1s, **(h)** carbon 1s, **(i)** silicon 2p, **(j)** Table representing surface composition in atomic percentages for each element in 3C-SiC and 3C-SiC-MnO_2.

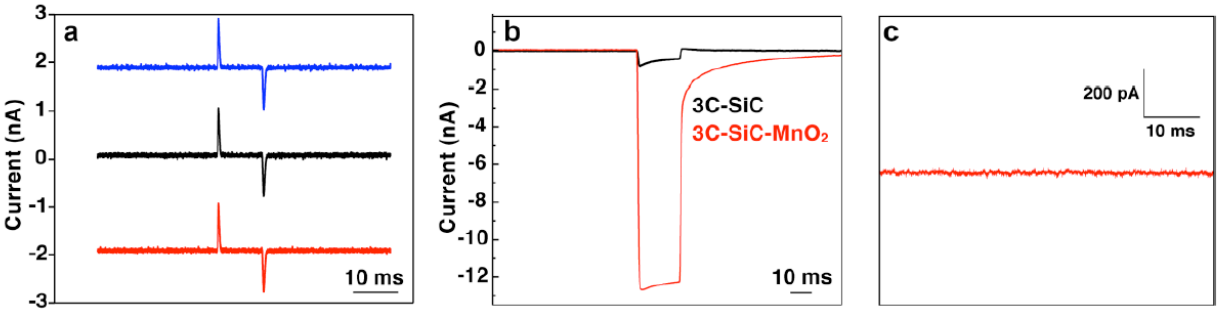

Fig. S6. Photoresponse measurements of intrinsic SiC, 3C-SiC-MnO$_2$ and backside graphite suggest faradaic activities from 3C-SiC-MnO$_2$. a. Photocapacitive response of intrinsic 3C-SiC wafer and its invariance with the bias of current injection. **b.** Surface modification of 3C-SiC by MnO$_2$ further enhances the photoanodic oxidation reaction as indicated by the magnitude difference in current. **c.** Absence of photoresponse from the graphite formed beneath SiC. (Stimulation: 350 nm/514.5 nm LED with a 10 ms pulse)

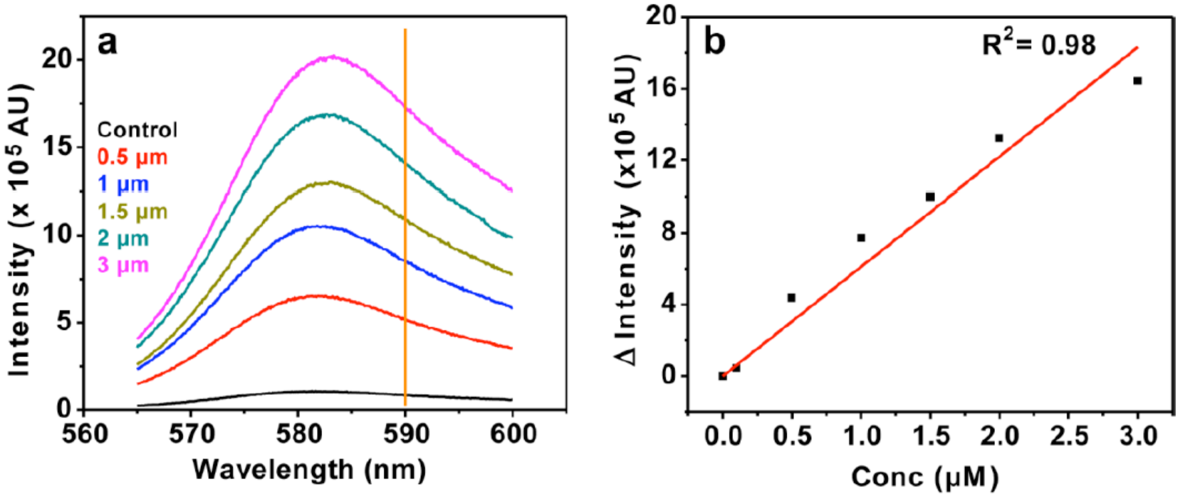

Fig. S7. Intensity versus concentration calibration of Amplex red dye. a. Steady state fluorescence of Amplex Red for specific concentration of hydrogen peroxide. Each curve is a separate measurement done with freshly mixed dye stock solution and hydrogen peroxide of an appropriate concentration. **b.** The intensity changes (from S7. a.) with respect to 0 mM hydrogen peroxide curve at 590 nm is plotted with respected to the added concentration of hydrogen peroxide. The curve fitted by least squares methods (R^2 = 0.98) gives a linear correlation between concentration change of hydrogen peroxide and the fluorescence intensity change for a fixed concentration of Amplex Red. This fitted curve is used a calibration curve to construct the quantitative fluorescence kinetics curve in main manuscript Fig. 5C.

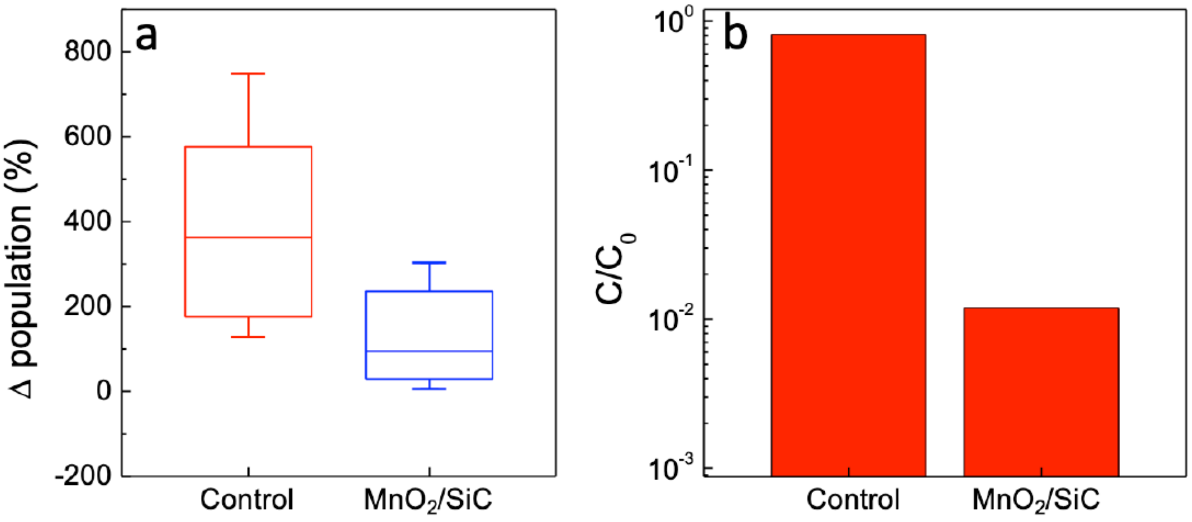

Fig. S8. Bacterial disinfection experiments show growth inhibition with white light illumination. a. Percentage change in bacterial population measured by standard spread plate culture, with photoelectrochemical anti-bacterial treatment of 3C-SiC-MnO_2 compared with samples containing 3C-SiC-MnO_2 under dark (N=15). **b.** Average fractional change in bacterial population (with respect to bacterial culture without any 3C-SiC-MnO_2 under light conditions), estimated by standard spread plate culture with photoelectrochemical anti-bacterial treatment of 3C-SiC-MnO_2 compared with samples containing 3C-SiC-MnO_2 under dark.

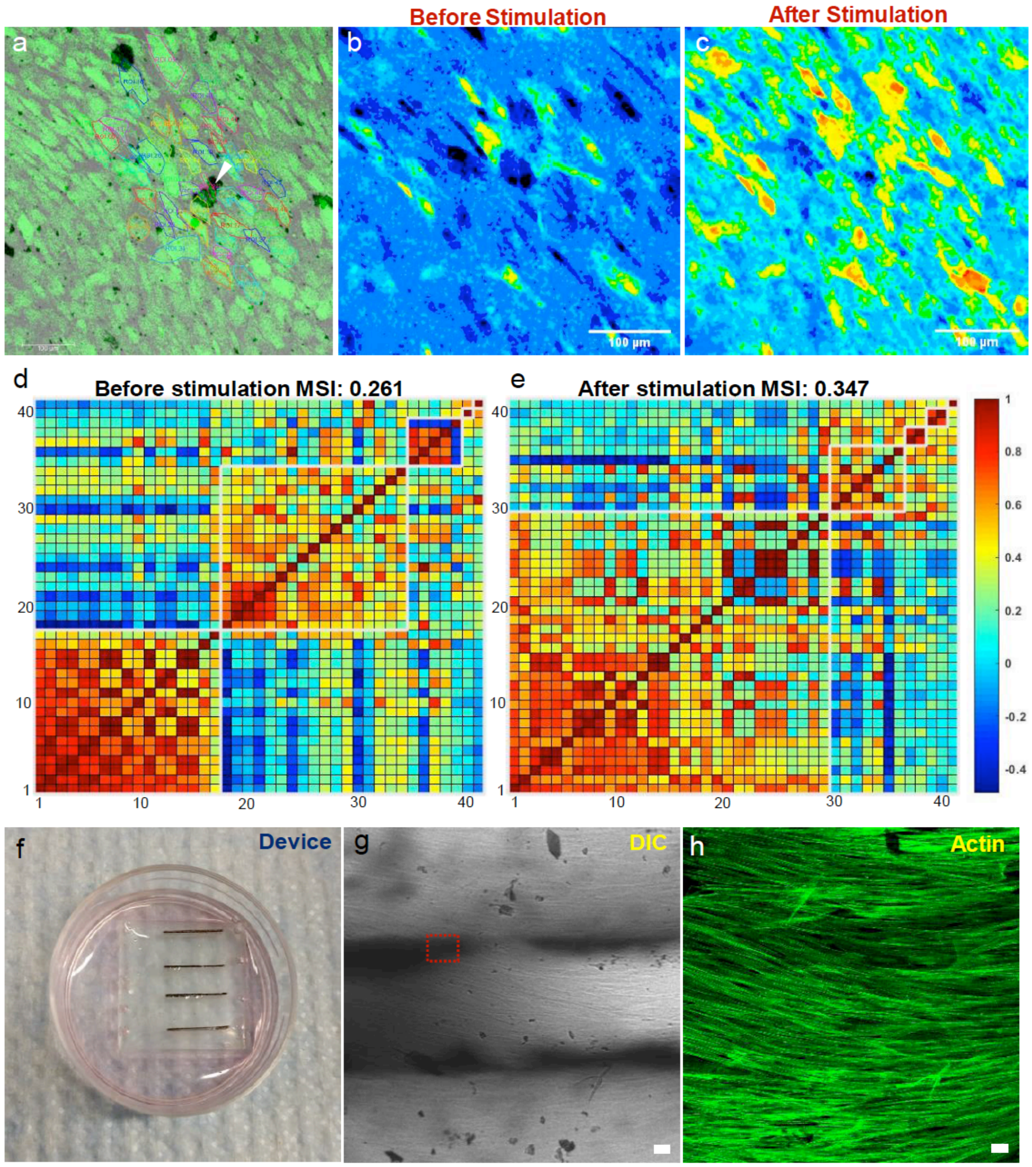

Fig. S9. Optical stimulation improves the synchronization of smooth muscle activities. a. Overlay of calcium and DIC image showing 3C-SiC particles co-cultured with smooth muscle cells along with stimulation point indicated as a white arrow. Region of interests (ROIs) used for synchronization analysis in a and b have been marked (Stimulation Power: 29 mW, Pulse: 1 ms). **b.** Differential calcium image (ΔF/F) of the smooth muscle cell sheet in (**a**) before stimulation**. c.** Differential calcium image (ΔF/F) of the smooth muscle cell sheet in (**a**) after stimulation revealing a global increase in calcium. **d.** Synchronization matrix of calcium signals before stimulation along with mean synchronization index (MSI) of 0.261 (X axis and Y axis are Neuron IDs). **e.** Synchronization matrix of calcium signals after stimulation along with mean synchronization index (MSI) of 0.347 (X axis and Y axis are Neuron IDs), (Stimulation Power: 29 mW, Pulse: 1 ms). HASMCs are cultured on the device **(f)** to obtain a uniform film of cells as observed through DIC image **(g),** Actin immunofluorescence staining **(h)**. The red box in (**g**) indicates the stimulation spot for Fig. 5g in main manuscript. Scale bars in (**g-h**) are 100 μm each. Photo credit for S9f: Vishnu Nair, University of Chicago.

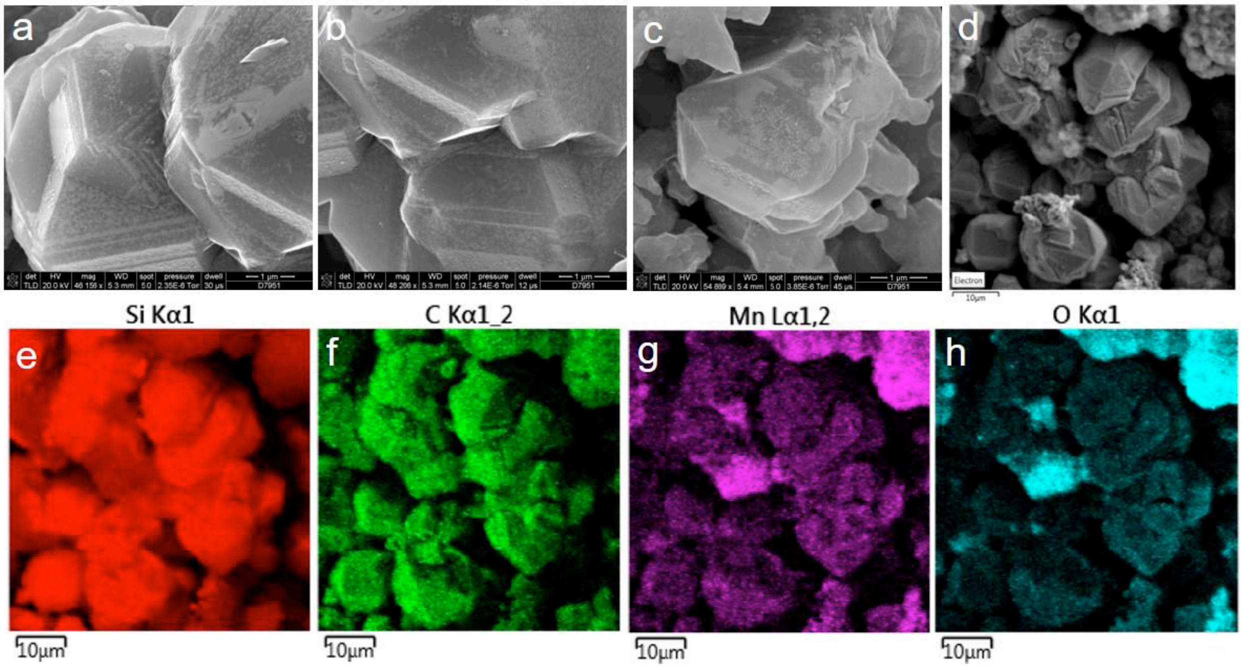

Fig. S10. SEM-EDS reveals the chemical composition of 3C-SiC-MnO$_x$. a-d. Magnified view of crystals showing a coating of MnO$_x$ (x~2), created with electroless deposition. **E-h.** EDS map of various elements on crystals shown in (**d**).

Supplementary Videos:

Video S1. **Differential calcium wave propagation on a smooth muscle cell layer from a stimulation point on a SiC/PDMS device**. (Corresponding to Fig. 5G, Stimulation Power: 8 mW, Pulse: 1 ms)

Video S2. Differential calcium wave propagation from a stimulation point on a smooth muscle cell layer co-cultured with SiC particles. (Corresponding to Fig. S9b and S9c, Stimulation Power: 29 mW, Pulse: 1 ms)